Solution-Phase Synthesis of Co-N-C Catalysts Using Alkali Metals-Induced N-C Templates with Metal Vacancy-N_x sites

Mengxue Huang[1,2], Lifang Chen[1], Ruimin Ding[1], Wenwen Shi[1], Qianqian Qin[1,2], Jie Yang[1,2], Shufang Shi[1,2], Shanshan Liu[1], Xi Yin[1]*

Affiliations:

[1]State Key Laboratory of Coal Conversion, Institute of Coal Chemistry, Chinese Academy of Sciences; Taiyuan, Shanxi 030001, China.

[2]School of Chemical Engineering, University of Chinese Academy of Sciences; Beijing 100049, China.

*Corresponding author. Email: xiyin@sxicc.ac.cn

Abstract

Nitrogen-coordinated metal sites (MN_x) in metal- and nitrogen-co-doped carbon (M-N-C) catalysts are known for their versatile and promising electrocatalytic activity. However, the synthesis of MN_x moieties with desired configuration and catalytic property is still quite challenging using the conventional high-temperature treatment approach. In this study, we demonstrate the solution-phase synthesis of Co-N-C catalysts via the formation of CoN_x moieties at metal vacancy-N_x (MVN_x) sites on nitrogen-doped carbon (N-C) templated by alkali metals, including sodium and potassium. The formation of CoN_x sites is confirmed via a combined approach of various physical characterization techniques, elemental analysis, and electrochemical analysis. For each series of Co-N-C catalysts templated by the same alkali metal (e.g., Na or K), there is a correlation between the CoN_x content and the electrocatalytic activity for the oxygen reduction reaction (ORR). Moreover, the correlation of CoN_x content with ORR activity also depends on the type of sacrificial alkali metals, suggesting the role of sacrificial metals in creating MVN_x sites with a diverse coordination environment. These findings may further guide the future development of M-N-C electrocatalysts with abundant and versatile MN_x moieties through this solution-phase coordination approach.

Introduction

With the development of the economy, the demand for energy supply and environmental control has increasingly become the inevitable driving force of the development of human society. In the past few decades, the development of advanced energy storage and conversion technologies has received more and more attention. Metal and nitrogen co-doped carbon (M-N-C) electrocatalysts with nitrogen-coordinated metal (MN_x) active sites have been widely studied for their promising electrocatalytic activity towards versatile reactions, such as the oxygen reduction reaction (ORR) for fuel cells,[1-3] the oxygen evolution reaction (OER) and hydrogen evolution reaction (HER) for water electrolysis,[4-7] and the CO_2 reduction reaction (CO_2RR) for the production of value-added chemicals.[8-11]

So far, a series of synthesis methods have been developed for M-N-C catalysts, including traditional pyrolysis method, self-sacrificing template method, chemical vapor deposition method, MOF-based encapsulation pyrolysis, etc.[2, 12-14] However, these synthesis methods largely rely on the high-temperature treatment step to form the MN_x active sites. The detailed mechanism of MN_x site-formation at high temperature is still elusive. Therefore, it is still challenging to synthesize M-N-C catalysts with the desired MN_x moieties and catalytic property. New synthetic strategies with more precisely controlled process need to be developed for the rational design of M-N-C catalysts.

Recently, the coordination synthesis of M-N-C electrocatalysts on nitrogen-doped carbon (N-C) templates with rich MN_x sites induced by sacrificial metals (SM) has received great attention.[15-23] The related works introduced SM to create SMN_x structures or metal-vacancy-N_x (MVN_x) sites on the carbon matrix, and then formed MN_x sites with high activity and site density via a wet-chemical metal-coordination step and high-temperature treatment. For instance, magnesium was used as a dual template to form Mg-N_4 sites by pyrolysis and generate graphitized carbon containing 43% "surface Fe-N_4" sites via a low-temperature transmetalation step.[17] Zinc is used as a sacrificial metal with MOF as the precursor, largely removed after high-temperature pyrolysis and washing, leaving empty N_x sites. Then the obtained sites were converted to the Fe-N_x sites with high ORR activity,[20] or by adsorption and heat-treatment to get the Ni-N_x sites with CO_2RR activity.[18] Another work also demonstrated the solution-phase metalation of MVN_4 sites in N-C support induced by zinc.[24] More recently, our group used Ni

to introduce MVN_x sites and synthesized Ni-MN_x-C catalysts (M = Co^{2+}, Fe^{2+}, Fe^{3+}) for ORR via a solution-phase coordination approach, without any further heat-treatment.[25]

It is not surprising to notice that these recent works using the solution-phase coordination methods mostly utilized sacrificial metal cations and target metal ions with the oxidation state of +2, including Zn^{2+}, Mg^{2+}, Ni^{2+}, Fe^{2+}, and Co^{2+}, for their similarity in terms of favored coordination configuration with the N_x-sites. However, it is still unclear whether MVN_x sites can form with sacrificial metals in other valence states. In light of general coordination chemistry, we think the types of the sacrificial metal cations may strongly affect the structures of induced SMN_x and MVN_x sites, thus determine the final form of MN_x sites in M-N-C catalysts and their electrocatalytic activity.[21, 26] Specifically, the SM cations with various valence states, ionic radius, and thermodynamically favored coordination configurations may induce a family of diverse MVN_x sites with specific population distributions.[25, 27] Therefore, one may use the SM cations to template the formation of MN_x sites with specific structures and properties.

Furthermore, the monovalent alkali metal ions can form stable coordination compounds with various types of nitrogen-containing ligands.[28-30] For instance, Li^+, Na^+ and K^+ ions can form porphyrins and other macrocyclic compounds. In these compounds, Li^+ tends to adopt an in-plane coordination configuration while Na^+ and K^+ tends to adopt an out-of-plane configuration for their larger ionic radius.[31-33] The arrangement of heterocyclic-N atoms in these compounds resembles the coordination environment of MN_x sites in the M-N-C catalysts. Therefore, it is possible to create alkali metal-N_x template sites via the heat-treatment of alkali metal salts and nitrogen-containing compounds.

Herein, we use alkali metal cations, including sodium (Na^+) and potassium (K^+) ions to direct the synthesis of N-C template with MVN_x sites, noted as Na-MVN_x-C and K-MVN_x-C templates, respectively. These MVN_x-C templates are further coordinated with target Co^{2+} metal ions in a solution-phase to synthesize a series of Co-N-C catalysts for the ORR. The formation of CoN_x moieties is confirmed via a combined approach of various physical characterization techniques, elemental analysis, and electrochemical analysis. For each series of Co-N-C catalysts templated by the same alkali metal (*e.g.*, Na or K), there is a correlation between the CoN_x content and their electrocatalytic activity for the ORR. Moreover, the

correlation of CoN_x content with the ORR activity also depends on the type of sacrificial alkali metals, suggesting the role of sacrificial metals in creating MVN_x sites with a diverse coordination environment. These findings may further guide the future development of M-N-C electrocatalysts with abundant and versatile MN_x moieties through this solution-phase coordination approach.

Experimental

Materials

Aniline (≥99.5%, Sigma-Aldrich), sodium chloride (NaCl, 99.99%, anhydrous, Aladdin, China), potassium chloride (KCl, 99.0–100.5%, anhydrous, Sigma-Aldrich), iron(II) chloride tetrahydrate ($FeCl_2·4H_2O$, 99.95%, Macklin, China), cobalt(II) chloride ($CoCl_2$, 99.7%, anhydrous, Macklin, China), ammonium persulfate (APS, 98%, reagent grade, Sigma-Aldrich), hydrochloric acid (HCl, 36–38 wt.%, analytical reagent grade, SCR, China), nitric acid (HNO_3, 65–68 wt.%, analytical reagent grade, SCR, China), isopropanol (IPA, >99.7%, analytical reagent grade, Kermel, China), methanol anhydrous (MeOH, ≥99.5%, analytical reagent grade, SCR, China), sulfuric acid (H_2SO_4, 95–98 wt.%, analytical reagent grade, SCR, China), deionized water (DI-water, Milli-Q, 18.2 MΩ cm at 25°C), ultrapure nitrogen (N_2, 99.999%), ultrapure oxygen (O_2, 99.999%), carbon black (BlackPearl 2000, Cabot Co.), a Nafion D521 dispersion (5 wt.%, EW = 1100, Alfa Aesar), PtRu-C (60 % PtRu on High Surface Area Carbon, Pt:Ru = 1:1, SCI Materials Hub), a alkaline dispersion (PiperION-A5-HCO3-EtOH, 5 wt.%, SCI Materials Hub), anion exchange membrane (PiperION-A type-HCO3, SCI Materials Hub) were used as received.

Synthesis of the Na-MVN_x-C and K-MVN_x-C templates

The Na or K-MVN_x-C templates were prepared by the heat treatment (HT) of a precursor containing sodium salt or potassium salt, a nitrogen-containing compound, and a carbon source. Specifically, OCB was first prepared by oxidizing 10.0 g of carbon black in 500 mL of 70% HNO_3 for 8 h at 80°C, rinsed with deionized (DI) water, vacuum dried at 80°C, and used as the carbon source in the synthesis. Next, aniline (2.048 g, 22 mmol) was dissolved in 200 mL of 1-M HCl solution to serve as the nitrogen source. NaCl (6.428 g, 110 mmol) and KCl (8.201

g, 110 mmol) were added to 200 mL of 1-M HCl solution containing the oxidizer APS (1.280 g, 5.5 mmol), respectively, as sodium and potassium sources for the polymerization of aniline. Then, the solution containing metal sources and oxidizer was slowly dropped into the aniline solution under magnetic stirring at 100 rpm and kept at room temperature with constant stirring for 2 hours to form a precursor solution. A carbon dispersion containing 0.4 g of OCB in a mixture of 100-mL DI-water and 10-mL IPA was then added to the above solution while stirring at 600 rpm to form a precursor mixture. After 24 h, the mixture was heated to 80°C and concentrated into a black slurry. The obtained slurry was then transferred into an alumina combustion boat and heat-treated in a quartz tube (inner diameter, 5.4 cm) furnace with N_2 flowing at 3 L/min. During the HT, the temperature was first raised to 600°C, 800°C, 900°C, or 1000°C at a heating rate of 30°C/min, then maintained for 1 h, and finally cooled naturally.

The obtained materials were ground into fine powders, then rinsed with DI-water, and vacuum dried to obtain the Na-MVN_x-C and K-MVN_x-C templates, which were noted as Na-MVN_x-C_*T* and K-MVN_x-C_*T* (*T* = 600°C, 800°C, 900°C, and 1000°C), where *T* represents the HT temperature.

Solution-phase coordination of Na-MVN_x-C and K-MVN_x-C templates with target metal ions

The synthesized Na-MVN_x-C and K-MVN_x-C templates were coordinated with target metal ions in the solution-phase. In a typical procedure, 0.1 g of Na-MVN_x-C_*T* and K-MVN_x-C_*T* templates material was added to 40 ml of methanol with 0.1-M anhydrous $CoCl_2$ dissolved in it. This mixture was then purged by bubbling N_2 for 10 min to remove any dissolved oxygen, sealed, and sonicated for 1 h. Then, the mixture was magnetically stirred at 400 rpm at 60°C for three days to enable the target metal ions to coordinate with the template. The mixture was then centrifuged and washed with methanol several times to completely remove the uncoordinated metal ions. Finally, the obtained catalyst was vacuum dried at 60°C, ground into a fine powder, and noted as Na-Co(II)N_x-C_*T* and K-Co(II)N_x-C_*T* .

Electrochemical measurements

Electrochemical measurements were conducted using a three-electrode system controlled by a

Pine Research MSR rotator (Pine Research Instrumentation Co. Ltd.) and a bipotentiostat (CHI 760E, CH Instruments, Inc.). A five-necked electrochemical cell filled with 0.1-M KOH solution was used in the experiment. A rotating-ring disk electrode (RRDE, Pine Research Instrumentation) with a glassy carbon electrode (GCE, Φ = 5.50 mm, area = 0.2375 cm^2) and a Pt-ring electrode were used as the working electrode. A graphite rod was employed as the counter electrode. A Hg/HgO electrode was used as the reference electrode under the alkaline electrolyte. The Hg/HgO electrode was calibrated to a reversible hydrogen electrode (RHE), which was constructed by bubbling pure H_2 gas continuously onto a Pt coil electrode placed in a glass tube filled with the electrolyte solution.

The catalyst ink was prepared by dispersing 5 mg of catalyst in a mixture of DI-water (500 μL), IPA (500 μL), and D521 Nafion dispersion (15 μL, 5 wt.%) in a sonication bath for one hour. Then, electrodes with a catalyst loading of 0.6 mg/cm^2 were prepared by depositing 28.9 μL of the ink onto the GCE on the RRDE.

Cyclic voltammograms (CVs) were recorded from 0 to 1.0 V *vs*. RHE at a scan rate of 50 mV/s in an N_2-saturated 0.5-M H_2SO_4 solution. The ORR performance was measured in O_2-saturated 0.5-M H_2SO_4 under steady-state conditions by polarizing the working electrode from 1.0 to 0 V *vs*. RHE using 20 mV potential steps and a hold time of 20 s at each step. The rotation rate was 900 rpm. The ring current was measured at a ring potential of 1.3 V *vs*. RHE. The ambient pressure in Taiyuan, Shanxi Province, China, is 92 kPa. The collection efficiency (N) of the RRDE electrode was measured to be 37%. The stoichiometric number of transferred electrons (n) in the ORR was calculated from the disk current (I_d) and ring current (I_r) results based on the following equation:

$$n = \frac{4I_d}{\left(I_d + \frac{I_r}{N}\right)} \qquad [1]$$

The kinetically limited current density (j_k) was determined using the Koutecký-Levich equation:

$$\frac{1}{j} = \frac{1}{j_k} + \frac{1}{j_d} \qquad [2]$$

Where j is the measured current density and j_d is the diffusion-limited current density.

The equation that governs j_d is

$$j_d = 0.62nFC_{O_2}D_{O_2}^{2/3}\nu^{-1/6}\omega^{1/2} \quad [3]$$

Where F is the Faraday constant, C_{O2} is the concentration of dissolved O_2, D_{O2} is the diffusion coefficient of O_2, ν is the kinematic viscosity of the electrolyte solution, and ω is the rotation rate of the disc electrode.

AEMFC Tests

The synthesized Na-Co(II)N_x-C_800 was applied as the cathode catalyst with the loading of 2.5 mg/cm^2. PtRu-C was used as the anode catalyst with the loading of 0.4 mg_{PtRu}/cm^2. The catalyst ink was prepared by ultrasonically dispersing the catalysts and ionomer into water and isopropanol. Then the catalyst ink was sprayed onto both sides of membrane to fabricate a catalyst-coated membrane (CCM) with the electrode area of 5 cm^2. All CCMs were immersed into 1-M KOH solution for 3 hours (exchange the solution every 1 hour) and then rinsed thoroughly with deionized water until the pH of the residual water was neutral. The obtained CCM was assembled with a fluorinated ethylene propylene (FEP) gasket, a gas diffusion layer (GDL, Sigracet 22 BB carbon paper), a graphite bipolar plate with 5 cm^2 flow field and a metal current collector for each side to complete the full AEMFC. The H_2-O_2 fuel cells were tested in Scribner 850e test station at a cell temperature of 95.5°C, an anode temperature of 89°C, and a cathode temperature of 97°C in H_2/O_2 flow at 1000 sccm and 1.25 bar backpressure.

Physical characterizations

The obtained materials were characterized using a high-resolution transmission electron microscope (HTEM, JEM-2100F, JEOL, Japan) equipped with an energy dispersive spectrometer (EDS) and a scanning electron microscope (SEM, JSM-7001F, JOEL, Japan). Powder X-ray diffraction patterns (XRD) were recorded using a Bruker D8-Advance-A25 diffractometer with CuKα radiation. Brunauer-Emmett-Teller (BET) surface area analysis was performed using a Micromeritics. Additionally, the chemical states of nitrogen and metal ions in the samples were analyzed by X-ray photoelectron spectroscopy (XPS, Kratos AXIS UL TRA DLD). The structural defects and the graphitization degree of the samples were analyzed by Raman spectra that were recorded on a LabRAM HR Evolution (HORIBA Scientific, France)

using a 514 nm laser as the excitation source.

Results and discussion

The morphology and composition of Na-MVN_x-C templates and Na-Co(II)N_x-C catalysts

Na-MVN_x-C templates were prepared by high-temperature pyrolysis of nitrogen precursors, as shown in Fig. 1a**.** First, sodium chloride (NaCl), aniline (ANI), and oxidized carbon black (OCB) were polymerized and concentrated into a dark slurry. Then the obtained slurry was pyrolyzed at different HT temperatures. The Na-MVN_x-C templates were then immersed in a methanolic solution of target metal chloride to form the Na / K-MN_x-C catalysts. We explore the morphology and composition analysis of Na-MN_x-C templates and Na-Co(II)N_x-C catalysts. SEM micrographs revealed that the tubular structure of the templates evolved into a granular shape gradually as the HT temperature increased, as shown in Fig. S1 and 1b. After the solution-phase Co^{2+} coordination treatment, the Na-Co(II)N_x-C catalysts inherited the carbon structures of the original Na-MVN_x-C templates, as shown in Fig. S2 and 1c. This result indicates that the solution-phase coordination process does not introduce any noticeable morphology change to the samples. Fig. 1d and S3 show the XRD patterns of the obtained Na-MVN_x-C template and Na-Co(II)N_x-C catalyst. There are two distinct characteristic peaks at around 26.2° and 44.3°, which are assigned to the (0 0 2) and (1 0 1) planes of the graphite phase (PDF #57-1621), respectively. No any miscellaneous peaks were observed. Fig. 1e and Fig. S4 show the high-resolution transmission electron microscope (HTEM) micrograph of the Na-MVN_x-C_1000 template and Na-Co(II)N_x-C_1000 catalyst without any nanoparticles observed. The EDS elemental mapping of C, N, Na, and Co reveals the uniform distribution throughout the carbon matrix in the Na-Co(II)N_x-C_1000 catalyst (Fig. 1f). And the high count of Co signal indicates the successful loading of highly dispersed Co.

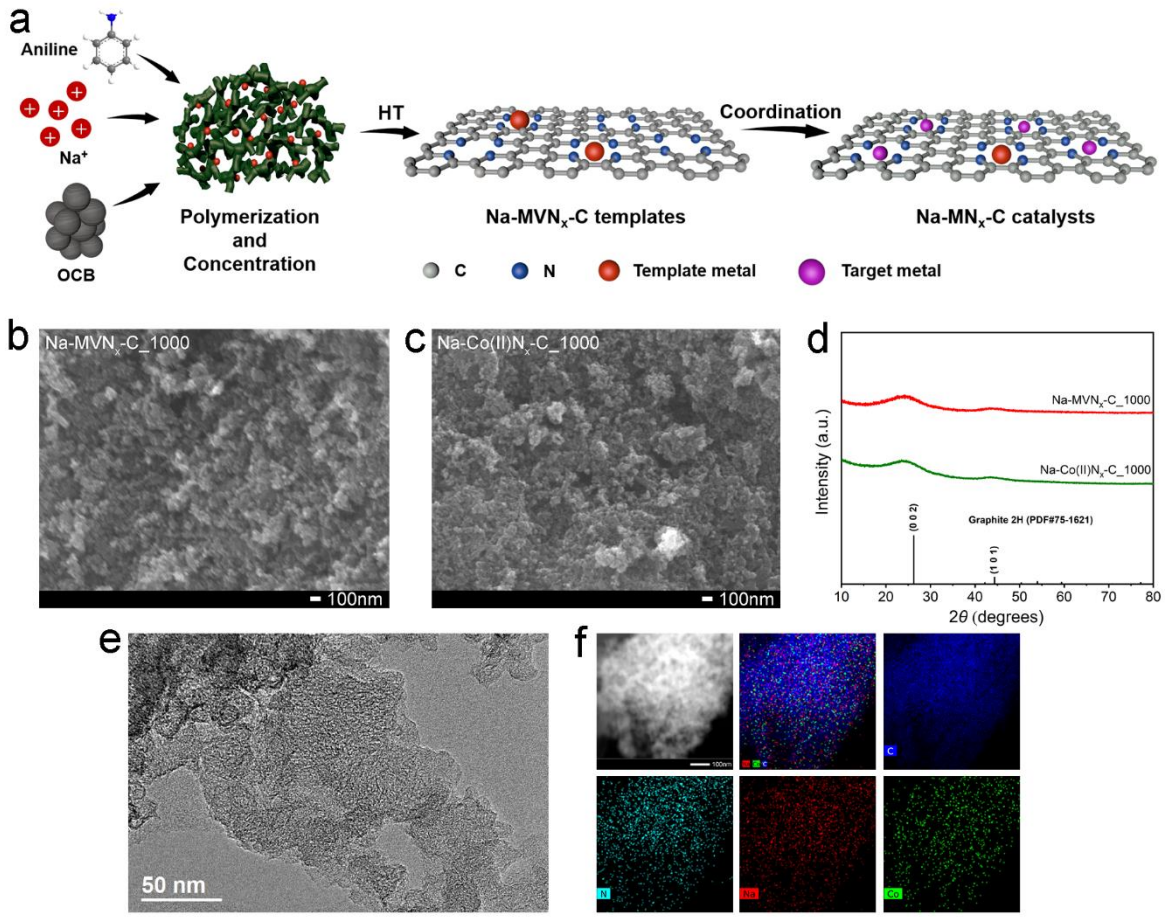

Fig. 1. (a) Synthesis scheme of the Na / K-Co(II)N_x-C catalysts by using Na / K-MVN_x-C templates. SEM micrograph of the (b) Na-MVN_x-C_1000 template and (c) Na-Co(II)N_x-C_1000 catalyst. (d) XRD patterns of Na-MVN_x-C_1000 template and Na-Co(II)N_x-C_1000 catalyst. (e) TEM micrograph of the Na-Co(II)N_x-C_1000. (f) HAADF-STEM and EDS elemental mapping of the Na-Co(II)N_x-C_1000.

The structural defects and the graphitization degree of the Na-MVN_x-C templates were investigated by Raman spectroscopy (Fig. S5). The D band (1360 cm^{-1}) and G band (1580 cm^{-1}) represent the disordered carbon (sp^3) and ordered graphitic carbon (sp^2), respectively[34, 35]. Fig. 2a shows that the intensity ratios I_D/I_G of Na-MVN_x-C_T (T = 600, 800, 900, 1000°C) templates are 1.14, 1.27, 1.04, 1.02, respectively. The Na-MVN_x-C_800 exhibited the largest value of I_D/I_G, indicating more defects in this carbon structure. The value of I_D/I_G decreases as the heat treatment temperature increases to 900, 1000°C, indicating that the graphitization of the templates increases. Fig. S6 shows the nitrogen isotherm of Na-MVN_x-C templates and

exhibits a classical IV adsorption−desorption isotherm and H3 hysteresis loop, illustrating the mesoporous character of obtained templates[36, 37]. The Na-MVN_x-C_ *T* (*T* = 600, 800, 900, 1000°C) templates exhibit specific surface areas of 288, 422, 482, and 374 m^2/g and pore volumes of 0.60, 0.79, 0.73, and 0.73 cm^3/g, as shown in Table S1.

The surface function of N plays an essential role in forming the active sites of ORR catalysts. The type and quantification of N sites in templates and catalysts were analyzed using XPS[34, 38]. Table S2 shows that the N content decreases with the increasing HT temperature, as some volatile N-containing substances will escape at elevated temperatures. Fig. S7 and 2b show the high-resolution N 1s XPS spectra of the Na-MVN_x-C templates and Na-Co(II)N_x-C catalysts, where similar N features are found in all materials, including pyridinic-N (398.4 eV), nitrogen coordinated with metal (M-N, 399.6 eV), pyrrolic-N (400.9 eV), graphitic-N (401.8 eV), and oxide-N (403.0 eV, 404.2 eV, and 405.3 eV) [39, 40]. Fig. 2c shows that the amount of N in M-N moieties in Na-MVN_x-C_*T* (*T* = 600, 800, 900, and 1000°C) templates are 1.32, 0.89, 0.75, and 0.41 at.%, respectively. After the solution-phase coordination, the amount of N in M-N moieties in Na-Co(II)N_x-C_*T* catalysts increased to 1.35, 1.01, 0.83, and 0.52 at.%, respectively. The increased amount of N in M-N moieties (ΔM-N) before and after Co^{2+} coordination was 0.03, 0.12, 0.08, and 0.10 at.%, indicating the successful formation of MN_x sites and the successful coordination of Co^{2+} on the MVN_x sites. The Co element content of Na-Co(II)N_x-C_*T* catalysts obtained by the XPS spectrum were 0.16, 0.40, 0.26, and 0.30 at.%, suggesting that the Co element was successfully loaded on the templates. According to the above Raman data and BET data analysis, the material exhibited more carbon defects, higher specific surface area and pore capacity, resulting in more significant ΔM-N and Co content when the HT temperature was 800°C. At the HT temperature of 600°C, minimal loaded and coordinated Co elements were found due to incomplete MV-N_x-C and low specific surface area. Fig. 2d shows the Na element content of 0.12, 0.27, 0.25, and 0.52 at.% in Na-MVN_x-C_*T* templates, and 0.09, 0.16, 0.18, and 0.39 at.% in Na-Co(II)N_x-C_*T* catalysts, respectively. The loss of Na element content decreased after coordination due to the possible ion exchange of Co^{2+} with Na^+ during coordination. The difference in the amount of ion exchange between Co^{2+} and Na^+ is related to the Na element content on the Na-MVN_x-C templates, and the more Na element content, the more likely to exchange with Co^{2+}. Fig. 2e exhibits that the process of

Co^{2+} coordination on the Na-MVN_x-C template involves both the coordination on the MVN_x sites and the ion-exchange process. These results suggest that the target metal can be successfully introduced to the templates via the simple solution-phase coordination step.

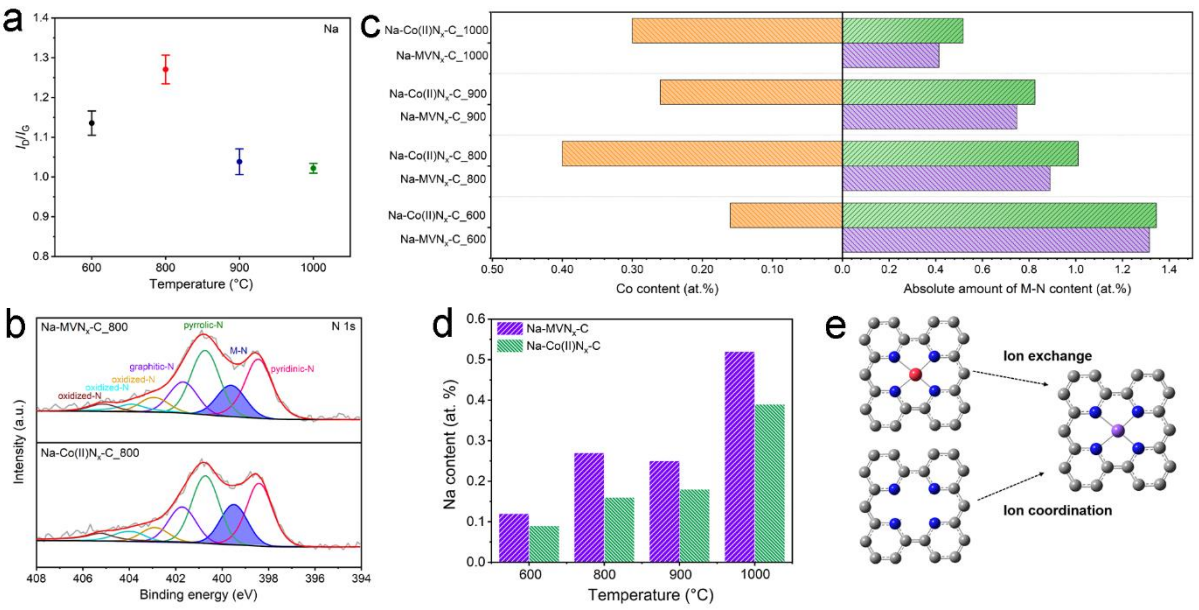

Fig. 2. (a) The integrated band ratio I_D/I_G from the Raman spectra of the Na-MVN_x-C templates obtained at different HT temperature. (b) Deconvoluted high-resolution N 1s XPS spectra of the Na-MVN_x-C_1000 template and Na-Co(II)N_x-C_1000 catalyst. (c) The absolute amount of M-N in Na-MVN_x-C templates and Na-Co(II)N_x-C catalysts, and Co content of Na-Co(II)N_x-C catalysts. (d) The Na content in Na-MVN_x-C templates and Na-Co(II)N_x-C catalysts. (e) The process of Co^{2+} coordination on the Na-MVN_x-C template.

The electrochemical behavior of Na-MVN_x-C templates and Na-Co(II)N_x-C catalysts

Since the Co-N_x sites are often used as active centers for ORR, we verified the formation of Co-N_x sites through electrochemical and AEMFC testing. Fig. S8 shows the CVs of the Na-MVN_x-C templates in alkaline media. Na-MVN_x-C_600 showed a very broad peak due to the pseudo-capacitance caused by the rich N-dopant species. However, this pseudo-capacitance peak decreased significantly with the increase in HT temperature. It is consistent with the lower nitrogen content because the incorporated N is the primary source of disorder in the graphite structure[41, 42]. Fig. 3a, 3b, and S9 depict steady-state ORR polarization curves of the Na-MVN_x-

C templates and Na-Co(II)N_x-C catalysts in alkaline media. Before Co^{2+} coordination, all templates exhibited low ORR activity with onset potentials of 0.81−0.85 V *vs.* RHE (η_{onset} at j = −0.05 mA/cm^2) and low kinetically limited current density of 0.10−0.50 mA/cm^2 at 0.8 V *vs*. RHE. After Co^{2+} coordination, the ORR performances improved significantly with the η_{onset} of 0.86−0.90 V *vs.* RHE. Especially for Na-Co(II)N_x-C_800 catalyst, the η_{onset} increase from 0.82 to 0.88 V *vs*. RHE, and the half-wave potential achieve 0.83 V *vs*. RHE. The increased oxygen reduction activity of the catalysts after Co^{2+} coordination indicates the successful formation of ORR-active Co-N_x sites.

Quantitative analysis in Fig. 3c revealed that there is a clear positive correlation between the increased amount in j_k (Δj_k) @0.8 V *vs*. RHE with the Co element content and the increase of N in M-N moieties before and after Co^{2+} coordination. The relationship between them can be described as the more loaded Co element content, the more Co-N_x sites formed after Co^{2+} coordination with the MVN_x sites, the greater the chance of forming the ORR-active Co-N_x sites, and the higher the oxygen reduction activity. To test the cell performance of the catalysts obtained after coordination, we selected the Na-Co(II)N_x-C_800 catalyst with the best oxygen reduction activity as the cathode of the anion exchange membrane fuel cell (AEMFC) for cell testing. Fig. 3d shows the polarization and power density curves of the AEMFC with the Na-Co(II)N_x-C_800 catalyst in the cathode. The AEMFC has an open-cell-voltage of 0.90 V and a maximum power density of 360 mA/cm^2. The result demonstrates better performance than previously reported in the literature for non-precious metal catalysts as the cathode[43-46]. The electrochemical and AEMFC tests fully reveal that the catalysts obtained via the solution-phase coordination have active MN_x sites to catalyze the oxygen reduction reaction.

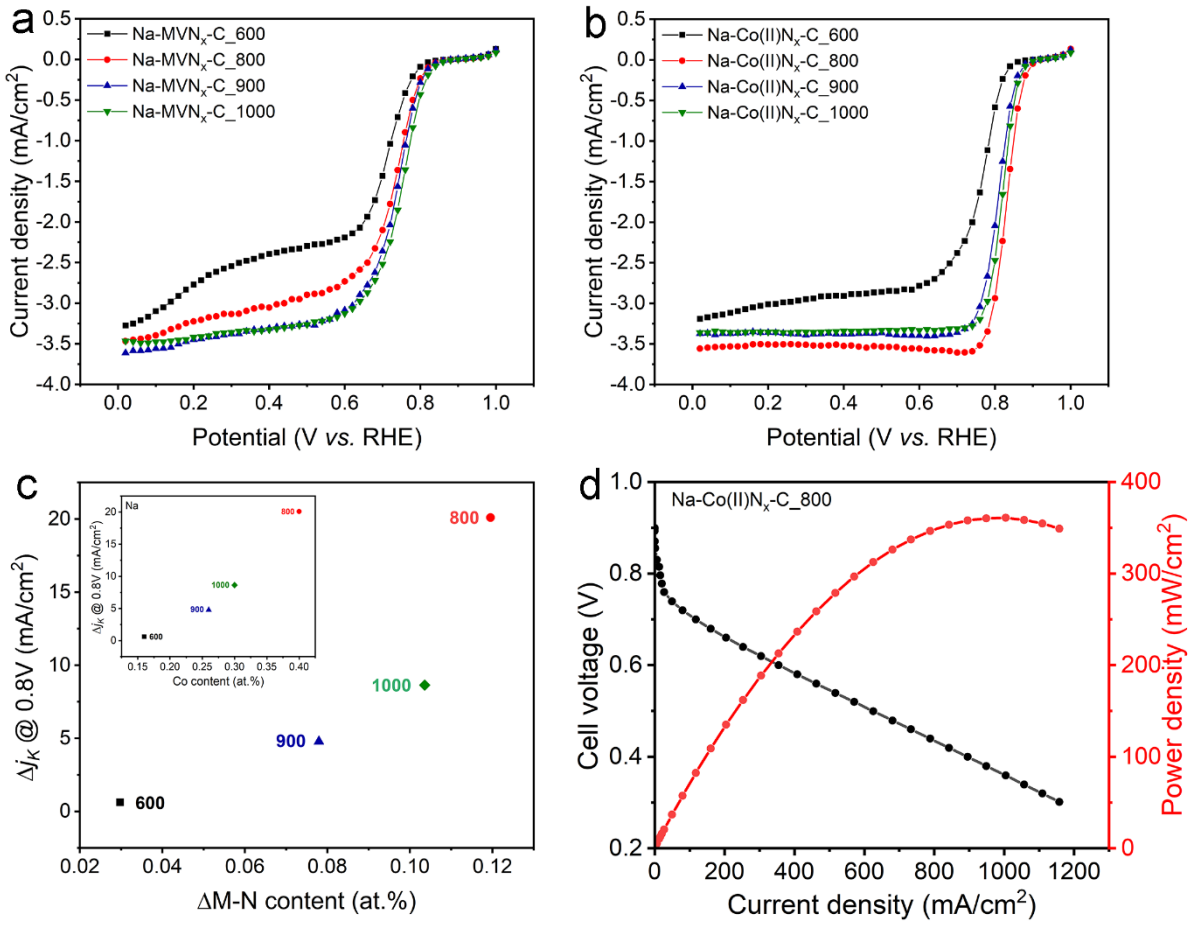

Fig. 3. Steady-state ORR polarization curves of (a) the Na-MVN$_x$-C templates, and (b) the Na-Co(II)N$_x$-C catalysts in O_2-saturated 0.1-M KOH. (c) Relationship between ΔM-N content and Δj_k @0.8 V *vs.* RHE on the Na-Co(II)N$_x$-C catalysts. (d) Polarization and power density curves for H_2-O_2 AEMFC with PtRu-C in anode and Na-Co(II)N$_x$-C_800 in cathode.

Effects of the sacrificial metal ion species on the activity of catalysts

In order to understand the effect of different sacrificial metals of the same main group on the coordination results, we used K as a sacrificial metal to form K-MVN$_x$-C templates and further obtained the K-Co(II)N$_x$-C catalysts via the Co^{2+} coordination step. Fig. 4a–c and S10-12 show that the structure without being significantly change after Co^{2+}coordination. The EDS elemental mapping observed the uniform dispersion of the Co elements, as shown in Fig. 4d. These results are similar to the Na-Co(II)N$_x$-C catalysts obtained using Na as a sacrificial metal, indicating that there is no significant effect on the catalyst morphology, no nanoparticles arise, and that Co^{2+} can be successfully loaded on the templates through the simple solution-phase

Co^{2+} coordination process. Fig. S13 and 4e show the Raman spectral peak fitting results of the K-MVN$_x$-C templates and the intensity ratios I_D/I_G. The I_D/I_G values of K-MVN$_x$-C_T (T = 600, 800, 900, 1000° C) templates are 1.16, 1.08, 1.07, and 1.04, respectively. The I_D/I_G values decrease as the temperature increases, indicating that the higher the HT temperature, the higher the degree of graphitization of the templates. Fig. 4f show that the increased amount of N in M-N moieties (ΔM-N) is 0.03, 0.05, 0.16, 0.12 at.%, respectively, and the Co element content is 0.20, 0.34, 0.41, 0.37 at.%, respectively. And more ΔM-N and Co content existed in K-Co(II)N$_x$-C_900.

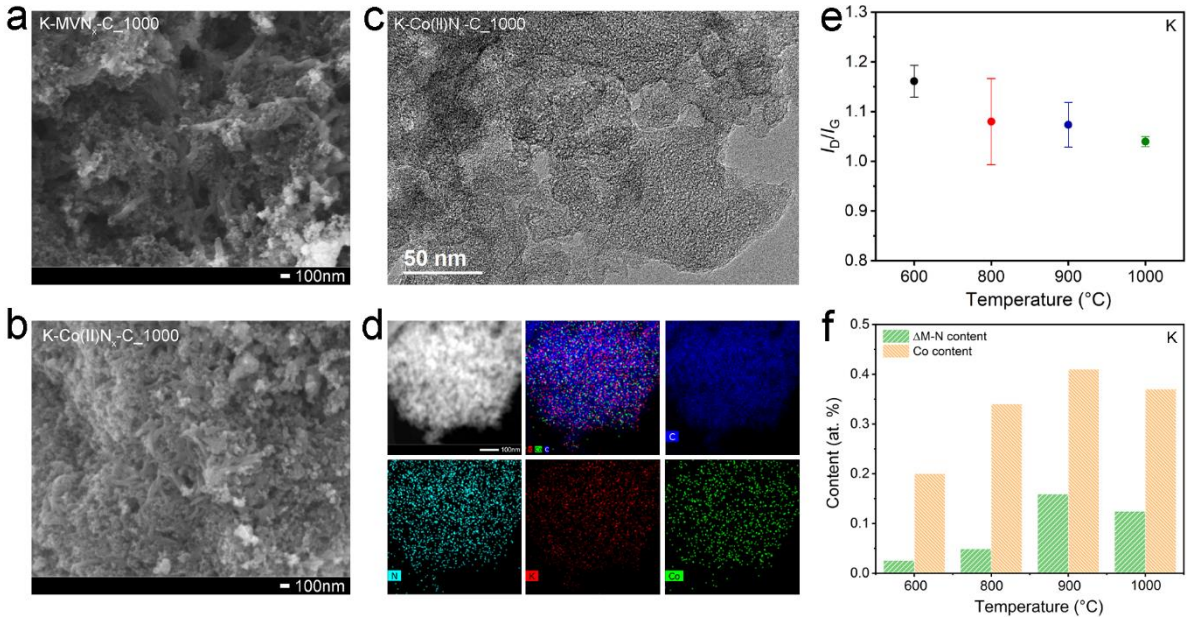

Fig. 4. SEM micrograph of the (a) K-MVN$_x$-C_1000 template and (b) K-Co(II)N$_x$-C_1000 catalyst. (c) TEM micrograph and (d) HAADF-STEM and EDS elemental mapping of the K-Co(II)N$_x$-C_1000. (e) The integrated band ratio I_D/I_G from the Raman spectra of the K-MVN$_x$-C templates obtained at different HT temperature. (f) The absolute amount of M-N and Co content of K-Co(II)N$_x$-C catalysts.

Similarly, we performed the electrochemical ORR tests on the K-MVN$_x$-C templates and K-Co(II)N$_x$-C catalysts. Fig. 5a shows that the K-MVN$_x$-C templates exhibited η_{onset} of 0.81−0.84 V *vs.* RHE and kinetically limited current density of 0.10−0.31 mA/cm^2 at 0.8 V *vs.* RHE. Fig. 5b shows that the η_{onset} of the K-Co(II)N$_x$-C catalysts increased to 0.85−0.89 V *vs.* RHE, and the half-wave potentials of the K-Co(II)N$_x$-C_T catalysts reached 0.75, 0.80, 0.82, 0.81 V *vs.* RHE, respectively. The relationship between the Δj_k @0.8 V *vs.* RHE and the ΔM-N content in Fig. 5c showed similar results to Na-Co(II)N$_x$-C catalysts, i. e., showing a

positive correlation. These findings indicate successful coordination of Co^{2+} on the templates and the formation of Co-N_x sites with ORR activity. The catalysts obtained after Co^{2+} coordination on the Na and K templates showed different activities, mainly attributed to the different the site density of the formed ORR-active MN_x sites and the species of the MN_x sites, and the species including the type of coordination nitrogen, the number of x, etc.

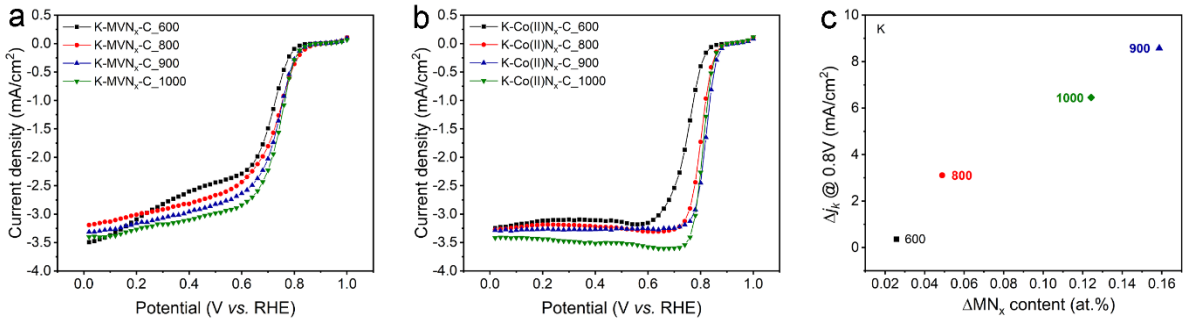

Fig. 5. (a) The comparison of the ΔM-N and Co content between K-Co(II)N_x-C catalysts and K-Co(II)N_x-C catalysts. Steady-state ORR polarization curves of (b) the K-MVN_x-C templates and (c) the K-Co(II)N_x-C catalysts. (d) Relationship between ΔMN_x content and Δj_k @0.8 V *vs.* RHE on K-Co(II)N_x-C catalysts.

Fig. 6a shows the comparison of Co content, ΔM-N and Δj_k between Na-Co(II)N_x-C_800 and K-Co(II)N_x-C_900 catalyst. The comparable Co content in the Na-Co(II)N_x-C_800 and K-Co(II)N_x-C_900 catalysts suggest closed number of Co-N_x active sites in the two catalysts, indicating that the SMN_x / MVN_x available template sites in K-MVN_x-C templates is close to Na-MVN_x-C templates. ΔM-N, the increased amount of N in M-N moieties represents the number of Co-N_x formed by coordination of Co^{2+} at the MVN_x template sites. The difference of ΔM-N between the two catalysts indicates that MVN_x sites in Na-MVN_x-C templates is lower than in the Na-MVN_x-C templates. In the previous discussion, we pointed out that in the Na-MVN_x-C template, there is an exchange between Co^{2+} and Na^+ in the SMN_x template site, while that is not present in the K-MVN_x-C template. This is why the ΔM-N of Na-Co(II)N_x-C_800 is lower that of K-Co(II)Nx-C_900, but a similar number of Co-N_x active sites for both of them. Therefore, for Na-Co(II)N_x-C_800 and K-Co(II)N_x-C_900 catalysts, although the numbers of active sits are close to each other, the coordination processes and environments of

the active sites are different. The higher ORR activity of Na-Co(II)N_x-C_800 than K-Co(II)N_x-C_900 catalyst is possible that the Co-N_x sites formed by SMN_x template sites is more active than those formed by MVN_x sites. As shown in Fig. 6b, the Co-N_x sites formed by SMN_x template sites is likely ORR-active MN_4 site; while Co-N_x sites formed by MVNx sites is likely ORR- less active MN_2C_2 or MN_3C_1 site. Regarding why NaN_4 can exchange with Co^{2+} but KN_4 cannot, we speculated that it is related to the thermodynamics and reaction kinetics of the system. In the following studies, we will continue to explore the effect of these unique coordination structures of sacrificial alkali metals on the ORR-active sites.

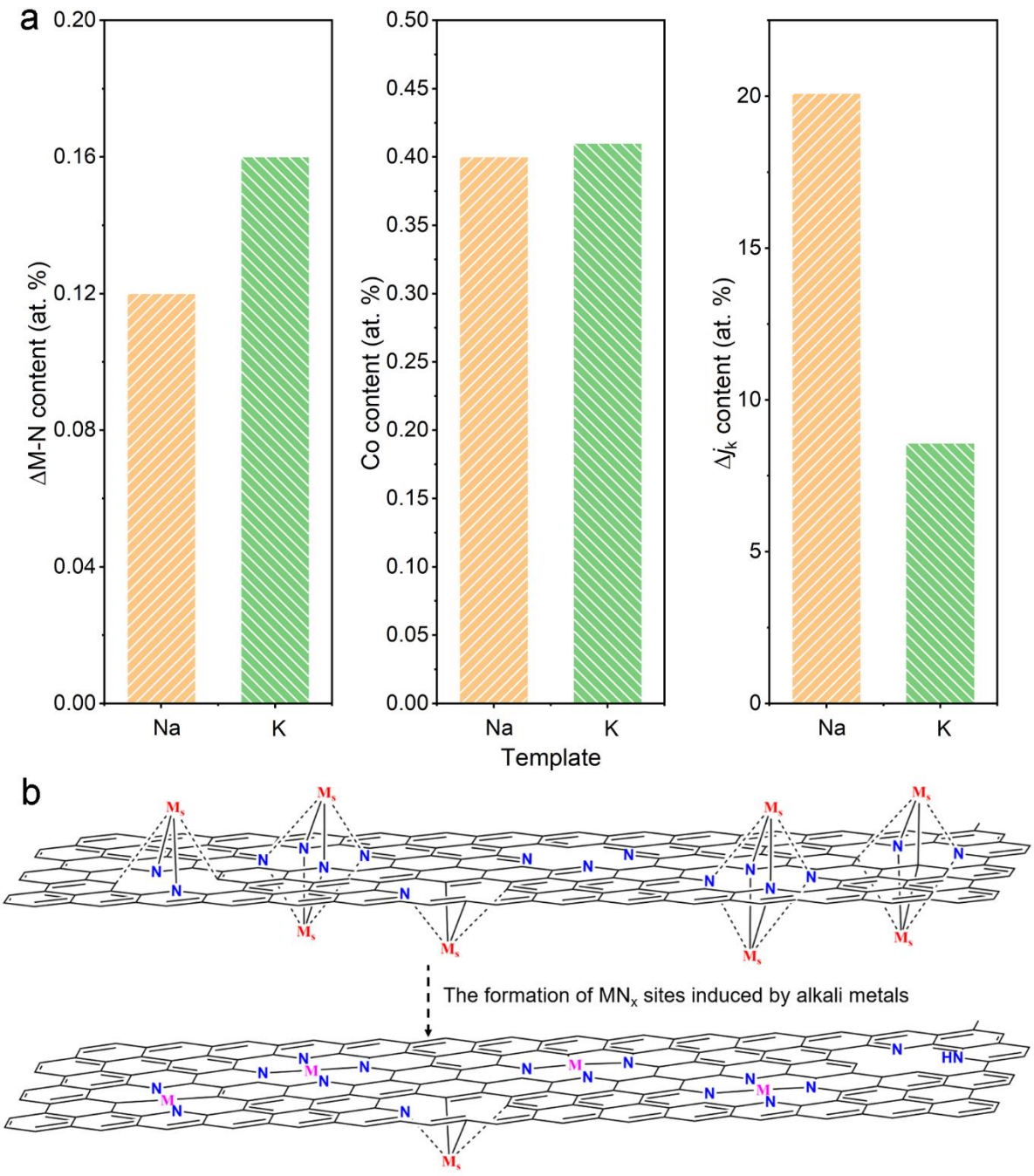

Fig. 6. (a) The comparison of the ΔM-N, Co content and Δj_k between Na-Co(II)N_x-C_800 and K-Co(II)N_x-C_900 catalysts. (b) The proposed mechanism for solution-phase synthesis of Co-N-C catalyst using alkali metals-induced MVN_x-C templates.

Conclusions

In summary, we synthesized Co-N-C catalysts by coordinating Co^{2+} ions with N-C templates containing MVN_x sites induced by alkali metal ions, including Na^+ and K^+. The increase of M-N content as quantified by the XPS analysis confirms the formation of CoN_x

moieties. By varying the heat-treatment temperatures, the amount of CoN_x moieties formed can be tuned for each group of samples synthesized using Na- or K-induced N-C templates. Moreover, the Co-N content correlates well with the increase of ORR activity after the formation of Co-N_x sites via the solution-phase coordination, with an elemental dependency on the alkali sacrificial metals. The Co-N-C catalysts synthesized using Na-MVN_x-C templates show higher ORR activity than those using K-MVN_x-C templates with similar content of Co-N. This work provides the basis for the rational design of M-N-C catalysts via this solution-phase coordination synthesis approach.

Acknowledgments

Financial support from the State Key Laboratory of Coal Conversion, Institute of Coal Chemistry, Chinese Academy of Sciences is greatly appreciated. This study was financially supported by the autonomous research project of Shanxi Province grant (Grant No. 20210302123011 and 202103021224442), SKLCC (Grant No. 2021BWZ006), ICC CAS (Grant No. 2020SC001), and Key Research and Development (R&D) Projects of Shanxi Province (202102070301018).

Associated content

Supplementary material. The Supplementary Material is available free of charge. Additional physical/electrochemical characterization data, Raman spectra, XPS spectra, SEM micrographs, and TEM micrographs (PDF).

References

1. J. Lilloja, E. Kibena-Poldsepp, A. Sarapuu, J. C. Douglin, M. Kaarik, J. Kozlova, P. Paiste, A. Kikas, J. Aruvali, J. Leis, V. Sammelselg, D. R. Dekel and K. Tammeveski, *ACS Catal*, **11**, 1920 (2021).
2. Y. Wang, X. Cui, L. Peng, L. Li, J. Qiao, H. Huang and J. Shi, *Adv Mater*, **33**, e2100997 (2021).
3. X. Wen, H. Qi, Y. Cheng, Q. Zhang, C. Hou and J. Guan, *Chinese Journal of Chemistry*, **38**, 941 (2020).
4. J. Chen, H. Li, C. Fan, Q. Meng, Y. Tang, X. Qiu, G. Fu and T. Ma, *Adv Mater*, **32**, e2003134 (2020).
5. F. Hu, H. Wang, Y. Zhang, X. Shen, G. Zhang, Y. Pan, J. T. Miller, K. Wang, S. Zhu, X.

Yang, C. Wang, X. Wu, Y. Xiong and Z. Peng, *Small*, **15**, e1901020 (2019).
6. Y. Ying, K. Fan, X. Luo, J. Qiao and H. Huang, *Journal of Materials Chemistry A*, **9**, 16860 (2021).
7. T. Sun, W. Zang, H. Yan, J. Li, Z. Zhang, Y. Bu, W. Chen, J. Wang, J. Lu and C. Su, *ACS Catalysis*, **11**, 4498 (2021).
8. C. Jia, S. Li, Y. Zhao, R. K. Hocking, W. Ren, X. Chen, Z. Su, W. Yang, Y. Wang, S. Zheng, F. Pan and C. Zhao, *Advanced Functional Materials*, **31**, 210707 (2021).
9. J. Leverett, J. A. Yuwono, P. Kumar, T. Tran-Phu, J. Qu, J. Cairney, X. Wang, A. N. Simonov, R. K. Hocking, B. Johannessen, L. Dai, R. Daiyan and R. Amal, *ACS Energy Letters*, **7**, 920 (2022).
10. H. B. Yang, S.-F. Hung, S. Liu, K. Yuan, S. Miao, L. Zhang, X. Huang, H.-Y. Wang, W. Cai, R. Chen, J. Gao, X. Yang, W. Chen, Y. Huang, H. M. Chen, C. M. Li, T. Zhang and B. Liu, *Nature Energy*, **3**, 140 (2018).
11. L. Zhao, Y. Zhang, L. B. Huang, X. Z. Liu, Q. H. Zhang, C. He, Z. Y. Wu, L. J. Zhang, J. Wu, W. Yang, L. Gu, J. S. Hu and L. J. Wan, *Nat Commun*, **10**, 1278 (2019).
12. J. Liu, Z. Jin, X. Wang, J. Ge, C. Liu and W. Xing, *Science China Chemistry*, **62**, 669 (2019).
13. Y. M. Zhao, P. C. Zhang, C. Xu, X. Y. Zhou, L. M. Liao, P. J. Wei, E. Liu, H. Chen, Q. He and J. G. Liu, *ACS Appl Mater Interfaces*, **12**, 17334 (2020).
14. Y. Zhu, B. Zhang, X. Liu, D. W. Wang and D. S. Su, *Angew Chem Int Ed Engl*, **53**, 10673 (2014).
15. T. Al-Zoubi, Y. Zhou, X. Yin, B. Janicek, C. Sun, C. E. Schulz, X. Zhang, A. A. Gewirth, P. Huang, P. Zelenay and H. Yang, *J Am Chem Soc*, **142**, 5477 (2020).
16. L. Jiao, J. Li, L. L. Richard, Q. Sun, T. Stracensky, E. Liu, M. T. Sougrati, Z. Zhao, F. Yang, S. Zhong, H. Xu, S. Mukerjee, Y. Huang, D. A. Cullen, J. H. Park, M. Ferrandon, D. J. Myers, F. Jaouen and Q. Jia, *Nat Mater*, **20**, 1385 (2021).
17. B. Koyuturk, E. M. Farber, F. E. Wagner, T.-P. Fellinger and D. Eisenberg, *Journal of Materials Chemistry A*, **10**, 19859 (2022).
18. Y. Li, N. M. Adli, W. Shan, M. Wang, M. J. Zachman, S. Hwang, H. Tabassum, S. Karakalos, Z. Feng, G. Wang, Y. C. Li and G. Wu, *Energy & Environmental Science*, **15**, 2108 (2022).
19. Y. Li, X. Liu, L. Zheng, J. Shang, X. Wan, R. Hu, X. Guo, S. Hong and J. Shui, *Journal of Materials Chemistry A*, **7**, 26147 (2019).
20. A. Mehmood, M. Gong, F. Jaouen, A. Roy, A. Zitolo, A. Khan, M.-T. Sougrati, M. Primbs, A. M. Bonastre, D. Fongalland, G. Drazic, P. Strasser and A. Kucernak, *Nature Catalysis*, **5**, 311 (2022).
21. A. Mehmood, J. Pampel, G. Ali, H. Y. Ha, F. Ruiz-Zepeda and T.-P. Fellinger, *Advanced Energy Materials*, **8**, 17017 (2018).
22. D. Menga, J. L. Low, Y. S. Li, I. Arcon, B. Koyuturk, F. Wagner, F. Ruiz-Zepeda, M. Gaberscek, B. Paulus and T. P. Fellinger, *J Am Chem Soc*, **143**, 18010 (2021).
23. D. Menga, F. Ruiz‐Zepeda, L. Moriau, M. Šala, F. Wagner, B. Koyutürk, M. Bele, U. Petek, N. Hodnik, M. Gaberščček and T. P. Fellinger, *Advanced Energy Materials*, **9**, 1902412 (2019).
24. J. S. Bates, F. Khamespanah, D. A. Cullen, A. A. Al-Omari, M. N. Hopkins, J. J. Martinez,

T. W. Root and S. S. Stahl, *J Am Chem Soc*, **144**, 18797 (2022).
25. M. Huang, R. Ding, J. Yang, W. Shi, S. Shi, L. Chen, S. Liu and X. Yin, *Journal of The Electrochemical Society*, **169**, 106507 (2022).
26. Y. Zhang, J. Yang, R. Ge, J. Zhang, J. M. Cairney, Y. Li, M. Zhu, S. Li and W. Li, *Coordination Chemistry Reviews*, **461**, 214493 (2022).
27. M. Ha, D. Y. Kim, M. Umer, V. Gladkikh, C. W. Myung and K. S. Kim, *Energy & Environmental Science*, **14**, 3455 (2021).
28. P. J. Brothers, *Advances in Organometallic Chemistry*, **48**, 289 (2001).
29. S. Yang, Y. Yu, X. Gao, Z. Zhang and F. Wang, *Chem Soc Rev*, **50**, 12985 (2021).
30. L. Zhao, D. Qi, L. Zhang, M. Bai and X. Cai, *Journal of Porphyrins and Phthalocyanines*, **16**, 927 (2012).
31. A. A.-S. Ali, J. Cipot-Wechsler, S. M. Crawford, O. Selim, R. L. Stoddard, T. S. Cameron and A. Thompson, *Canadian Journal of Chemistry*, **88**, 725 (2010).
32. P. J. Brothers, R. West and A. F. Hill, *Advances in Organometallic Chemistry*, **40**, 289 (2001).
33. H. L. Buckley and J. Arnold, *Dalton Transactions*, **44**, 30 (2015).
34. X. Wang, J. Zhou, H. Fu, W. Li, X. Fan, G. Xin, J. Zheng and X. Li, *J. Mater. Chem. A*, **2**, 14064 (2014).
35. D. Xu, Y. Fu, D. Xiao, X. Li, Y. Wang, K. Li, Z. Li, L. Zheng and X. Zuo, *RSC Adv*, **11**, 8437 (2021).
36. X. Dong, J. Wang, X. Wang, J. Xu, J. Yang, W. Zeng, Y. Zhang, G. Huang, J. Wang and F. Pan, *ACS Applied Energy Materials*, **5**, 12272 (2022).
37. C. Shao, L. Wu, H. Zhang, Q. Jiang, X. Xu, Y. Wang, S. Zhuang, H. Chu, L. Sun, J. Ye, B. Li and X. Wang, *Advanced Functional Materials*, **31**, 2100833 (2021).
38. M. Qiao, Y. Wang, Q. Wang, G. Hu, X. Mamat, S. Zhang and S. Wang, *Angew Chem Int Ed Engl*, **59**, 2688 (2020).
39. J. Yang, J. Li, R. Ding, C. Liu and X. Yin, *Journal of The Electrochemical Society*, **168**, 096502 (2021).
40. X. Yin, H. T. Chung, U. Martinez, L. Lin, K. Artyushkova and P. Zelenay, *Journal of The Electrochemical Society*, **166**, F3240 (2019).
41. Y.-H. Lee, K.-H. Chang and C.-C. Hu, *Journal of Power Sources*, **227**, 300 (2013).
42. M. Yang and Z. Zhou, *Adv Sci (Weinh)*, **4**, 1600408 (2017).
43. W. da Silva Freitas, B. Mecheri, C. Lo Vecchio, I. Gatto, V. Baglio, V. C. A. Ficca, A. Patra, E. Placidi and A. D'Epifanio, *Journal of Power Sources*, **550**, 232135 (2022).
44. Y. J. Sa, D. J. Seo, J. Woo, J. T. Lim, J. Y. Cheon, S. Y. Yang, J. M. Lee, D. Kang, T. J. Shin, H. S. Shin, H. Y. Jeong, C. S. Kim, M. G. Kim, T. Y. Kim and S. H. Joo, *J Am Chem Soc*, **138**, 15046 (2016).
45. A. Sarapuu, E. Kibena-Põldsepp, M. Borghei and K. Tammeveski, *Journal of Materials Chemistry A*, **6**, 776 (2018).
46. A. Sokka, M. Mooste, M. Käärik, V. Gudkova, J. Kozlova, A. Kikas, V. Kisand, A. Treshchalov, A. Tamm, P. Paiste, J. Aruväli, J. Leis, A. Krumme, S. Holdcroft, S. Cavaliere, F. Jaouen and K. Tammeveski, *International Journal of Hydrogen Energy*, **46**, 31275 (2021).